

Magnetic structure of holmium-yttrium superlattices

D. A. Jehan, D. F. McMorro, R. A. Cowley, R. C. C. Ward, M. R. Wells, and N. Hagmann
Oxford Physics, Clarendon Laboratory, Parks Road, Oxford OX1 3PU, United Kingdom

K. N. Clausen

Risø National Laboratory, Roskilde DK 4000, Denmark

(Received 17 November 1992)

We present the results of a study of the chemical and magnetic structures of a series of holmium-yttrium superlattices and a 5000 Å film of holmium, all grown by molecular-beam epitaxy. By combining the results of high-resolution x-ray diffraction with detailed modeling, we show that the superlattices have high crystallographic integrity: the structural coherence length parallel to the growth direction is typically ≈ 2000 Å, while the interfaces between the two elements are well defined and extend over approximately four lattice planes. The magnetic structures were determined using neutron-scattering techniques. The moments on the Ho^{3+} ions in the superlattices form a basal-plane helix. From an analysis of the superlattice structure factors of the primary magnetic satellites, we are able to determine separately the contributions made by the holmium and yttrium to the total helical turn angle per bilayer. It is found that the effective turn angle per atomic plane in the yttrium, which has a value of approximately 50° , is independent of both temperature and the number of yttrium or holmium planes. The turn angle in the holmium blocks changes with temperature, and always has a value that is greater than in bulk holmium. The variation in the turn angle with temperature depends on the length of the holmium block, but is largely independent of the thickness of the yttrium block. At low temperatures, the $(1/6)\mathbf{c}^*$ phase found in bulk holmium is suppressed. The observation of high-order magnetic satellites indicates that the moments instead form long-period, commensurate spin-slip structures. The results are discussed in terms of the strain present in these samples.

I. INTRODUCTION

The application of molecular-beam epitaxial (MBE) growth techniques to the fabrication of metallic crystals has opened up new areas of research in rare-earth magnetism. The control which is now achievable in the growth of superlattices allows samples with preselected numbers of atomic planes to be grown, with well-defined interfaces between blocks of the different materials. This provides a unique method of producing single crystals that are model magnetic systems, thus allowing fundamental theories of magnetism to be tested, and hence information about the intrinsic magnetism of the bulk metals to be learned.

Several rare-earth superlattice systems have already been the subject of detailed studies, and a thorough review of this work has been given by Majkrzak *et al.*¹ Here we summarize the results which are relevant to our study. Although work has been reported on systems composed of two magnetic materials, such as the Dy/Gd system,² most effort so far has gone into investigating superlattices where successive blocks of the magnetic material are separated by blocks of nonmagnetic yttrium. These include Dy/Y (Ref. 3) and Er/Y,⁴ and it is this type of system that we consider in this paper. The most important feature of the magnetism of these superlattices is that, for samples with the growth direction parallel to the c axis, there is coherence in the ordering between

adjacent blocks of magnetic material. In Dy/Y superlattices, for example, both the chirality and phase of the helical ordering in each Dy block is maintained across the Y blocks, and indeed the magnetic coherence length may extend to many bilayers. However, the Y block does not simply act as an inert spacer between the blocks of magnetic material. Instead it is found that there is a phase shift, proportional to the length of the Y block, introduced between neighboring Dy blocks. The exact mechanism by which the magnetic ordering is transmitted across the Y blocks is not understood. Suggestions have included the stabilization of a helical spin-density wave in the conduction band of the Y,³ and the possibility that the coupling between the Dy moments in different blocks by the Y conduction electrons is similar to the long-range Ruderman-Kittel-Kasuya-Yosida exchange interaction found in the bulk rare-earth metals.⁵

Another feature common to both Dy/Y and Er/Y superlattices is the suppression of phase transitions that occur in the bulk magnetic materials. This has been linked to the strain present in these systems. In bulk Dy there is a first-order transition from helical to ferromagnetic ordering at 85 K.⁶ This is magnetoelastically driven; there is an orthorhombic distortion of the crystal that changes the basal-plane lattice parameters. But in Dy/Y superlattices or Dy films grown on Y, the transition to ferromagnetic alignment occurs at a much reduced temperature or is completely suppressed⁷ because

the basal plane of the magnetic material is clamped by the Y. Bulk Er exhibits a transition to a cone phase at ≈ 18 K. This is again magnetoelastically driven, but the mechanism is slightly different to that causing the transition in Dy, in that it is caused by the strain dependence of the two-ion couplings. The lattice mismatch between Er and Y is sufficiently large that the clamping suppresses the conical phase at 10 K in Er films up to 14000 Å thick.⁸

Here we report on the results of a study of the magnetic structure of a series of seven Ho/Y superlattices. The magnetic structure of three Ho/Y superlattices has been investigated by Bohr *et al.*⁹ Combining neutron-scattering data with mean-field calculations, they proposed a model for the low-temperature magnetic structure of a Ho block of finite length that is different from the magnetic structure of the bulk in two respects. First, if the block of Ho contains nine atomic planes or fewer, then ferromagnetic ordering of the moments is favored instead of the basal-plane helical state. Second, in thicker blocks the moments are arranged in pairs about the six easy axes, except at the ends of a block where there is a tendency for the moments to align ferromagnetically. They were unable to establish conclusively the nature of the coupling across the Y blocks, but they suggested that the Ho blocks were antiferromagnetically coupled across thin Y blocks. Our motivation in making a more extensive investigation of this system was driven by the resurgence of interest in the magnetic structures of the heavy rare-earth metals, including the discovery of long-period commensurate magnetic structures in the spin-slip phase of Ho.^{10,11} We aimed to investigate whether spin-slip structures are formed in the superlattices, to study how they differ from those observed in the bulk, and to determine the nature of the coupling across the Y blocks.

In Sec. II we outline the relevant theory of x-ray and neutron scattering as applied to superlattices and describe the models we have developed to analyze our results. We then detail in Sec. III aspects of the sample growth and the results of our x-ray diffraction study of the samples. The findings of our neutron-scattering experiments are presented in Sec. IV. These are discussed in Sec. V, where we consider the effect of strain on the magnetic structures. Finally, Sec. VI is a summary of the results.

II. THEORY OF SCATTERING FROM SUPERLATTICES

A. X-ray scattering

The intensity of the elastic scattering of x rays from a crystal lattice may be written as

$$I(\mathbf{Q}) \propto \left| \sum_l f_l(\mathbf{Q}) e^{i\mathbf{Q}\cdot\mathbf{R}_l} \right|^2, \quad (1)$$

where \mathbf{Q} is the wave-vector transfer, \mathbf{R}_l is the position of the l th atom, $f_l(\mathbf{Q})$ is the scattering amplitude of the l th atom, and the sum is made over all atomic planes in the

superlattice. The functional form of the \mathbf{Q} dependence of $f_l(\mathbf{Q})$ is given in Ref. 12. For scans of the wave-vector transfer along the c axis we may, for a superlattice crystal, rewrite Eq. (1) as

$$I(Q) \propto \left| \left(\sum_{S=1}^N e^{iQLS} \right) \left(\sum_{l=0}^{n_{\text{Ho}}+n_{\text{Y}}-1} f_l(Q) e^{iQR_l} \right) \right|^2, \quad (2)$$

where there are N bilayers of length L , and n_{Ho} and n_{Y} are the number of atomic planes of Ho and Y in a single bilayer. The first term generates a series of peaks at positions given by $Q = (2\pi m/L)$, where m is an integer. The amplitude of these peaks is modulated by the more slowly varying envelope of the second term, the one-bilayer structure factor. To calculate this structure factor we need to know the l dependence of $f_l(Q)$ and R_l . In a real superlattice there will be surface roughness and interdiffusion of the two materials at the interfaces during growth, so the boundaries between the two materials will not be perfectly sharp. A number of functions have been used to model the concentration profile across the interface, including error functions¹³ and a damped square wave.³ We have used tanh functions: these also have the required shape, with an almost-linear variation at the middle of the interface and more rounding at the edges, but are simpler to use in computation. The expression for the concentration of Ho in the l th layer in a bilayer, where l runs from 0 to $(n_{\text{Ho}} + n_{\text{Y}} - 1)$, is

$$c_{\text{Ho}}(l) = \frac{1}{2} \{ 1 + \tanh[(l + 0.5)/\lambda_1] - \tanh[(l + 0.5 - n_{\text{Ho}})/\lambda_1] + \tanh[(l + 0.5 - n_{\text{Ho}} - n_{\text{Y}})/\lambda_1] \}, \quad (3)$$

where λ_1 is a measure of the width of the interface. The scattering amplitude of the l th layer is then given by

$$f_l(Q) = c_{\text{Ho}}(l) f_{\text{Ho}}(Q) + [1 - c_{\text{Ho}}(l)] f_{\text{Y}}(Q). \quad (4)$$

The spacing between the atomic planes is given by a similar expression, but with a slight change to the arguments of the tanh functions to ensure they are now centered at atomic positions rather than interatomic sites. Thus if we write

$$g_{\text{Ho}}(l) = \frac{1}{2} \{ 1 + \tanh(l/\lambda_2) - \tanh[(l - n_{\text{Ho}})/\lambda_2] + \tanh[(l - n_{\text{Ho}} - n_{\text{Y}})/\lambda_2] \}, \quad (5)$$

then the d spacings are given by

$$d_l = g_{\text{Ho}}(l) d_{\text{Ho}} + [1 - g_{\text{Ho}}(l)] d_{\text{Y}}, \quad (6)$$

where d_{Ho} and d_{Y} are the d spacings in the middle of a large Ho or Y block. The position of the l th atom is then

$$R_l = \sum_{m=0}^l d_m. \quad (7)$$

Note that the interface parameter is not the same for the concentration and d -spacing profiles, as the two may not necessarily vary in the same way in the interface region: even for a sharp interface there may be strain for

the atoms near the boundary, because the two materials must be lattice matched in the plane at the interface. To include half-integer planes and preserve the correct periodicity we simply extend our basic unit to two bilayers, find forms for the concentrations analogous to those in Eqs. (3) and (5), and perform the sum over S in Eq. (2) to $N/2$ instead of N . Similar calculations can be performed for other rational fractions of planes, but for irrational fractions the system is no longer periodic. Extending the repeat unit to be longer than one bilayer generates extra Bragg peaks, but the new structure factor ensures that these are negligibly weak.

There are three corrections factors that have to be made when comparing the calculated intensities to the measured values: the Lorentz factor, an absorption factor to account for attenuation of the x rays, and a polarization factor. The average values of n_{Ho} , n_{Y} , d_{Ho} , and d_{Y} and values of the interface parameters may then be obtained from a least-squares fit to the measured scattering profile.

B. Neutron scattering

When using neutrons as a probe there are both nuclear and magnetic scattering processes to consider. The nuclear scattering intensity has a functional form similar to that in Eq. (1), but with the appropriate nuclear scattering lengths in the place of the x-ray form factors. Here we are primarily concerned with the magnetic scattering. If the moments at site l have components $\langle J_{\alpha l} \rangle$, the intensity of the elastic scattering is

$$I_{\text{mag}}(\mathbf{Q}) \propto |F(Q)|^2 \sum_{\alpha, \beta} (\delta_{\alpha\beta} - \hat{\mathbf{Q}}_{\alpha} \cdot \hat{\mathbf{Q}}_{\beta}) \mathbf{S}^{\alpha\beta}(\mathbf{Q}). \quad (8)$$

In Eq. (8), $\hat{\mathbf{Q}}_{\alpha} = \mathbf{Q}_{\alpha} / |\mathbf{Q}|$, $F(Q)$ is the magnetic form factor, and the static spin-spin correlation function is given by

$$\mathbf{S}^{\alpha\beta}(\mathbf{Q}) = \frac{1}{N} \left| \sum_{ll'} \langle J_{\alpha l} \rangle \langle J_{\beta l'} \rangle e^{i(\mathbf{R}_l - \mathbf{R}_{l'}) \cdot \mathbf{Q}} \right|^2. \quad (9)$$

In our experiments the wave-vector transfer was usually parallel to the c axis, so taking this as the z direction we have

$$I_{\text{mag}}(\mathbf{Q}) \propto |F(\mathbf{Q})|^2 [\mathbf{S}^{xx}(\mathbf{Q}) + \mathbf{S}^{yy}(\mathbf{Q})]. \quad (10)$$

For a basal-plane helix $\mathbf{S}^{xx}(\mathbf{Q}) = \mathbf{S}^{yy}(\mathbf{Q})$. If β_l is the phase of the l th layer and the first moment lies along the positive- x axis then $\langle J_{xl} \rangle = \frac{1}{2} J_l (e^{i\beta_l} + e^{-i\beta_l})$. Thus the expression for the intensity becomes

$$I_{\text{mag}}(Q) \propto |F(Q)|^2 \left[\left(\sum_l J_l e^{i(QR_l - \beta_l)} \right)^2 + \left(\sum_l J_l e^{i(QR_l + \beta_l)} \right)^2 \right]. \quad (11)$$

Here l is summed over all planes in the superlattice. To simplify this expression further, we follow the factoriza-

tion procedure used for the x-ray scattering to give

$$\sum_l J_l e^{i(QR_l \pm \beta_l)} = \sum_{m=1}^N e^{i(QLm \pm \Phi)} \times \sum_l^{\text{one bilayer}} J_l e^{i(QR_l \pm \beta_l)}, \quad (12)$$

where Φ is the total phase shift across one bilayer. To evaluate the one-bilayer structure factor we need to have functional forms for the l dependence of J_l , R_l , and β_l that take into account the imperfect interfaces. For computational convenience we again use a tanh function to model the concentration profile in the interface region, but we make a few changes to the procedure adopted for the x-ray analysis.

The model adopted for calculating the magnetic one-bilayer structure factor takes as the origin the central atom in a Ho block. The sum for the magnetic scattering then gives a real amplitude

$$A_{\pm}(Q) = \sum_l^{\text{one bilayer}} J_l e^{i(QR_l \pm \beta_l)} = J_0 + \sum_l J_l \cos(\phi_l^{\pm}), \quad (13)$$

where $\phi_l^{\pm} = (QR_l \pm \beta_l)$. The sum is taken over sites l sufficient to sum over one bilayer. The model assumes that the magnetic moment in the center of the Ho block is A_H and zero in the Y block (neglecting any contribution from the conduction electrons to the moment), so that

$$J_l = \frac{A_H}{2} \{1 - \tanh[(l - I)/\lambda_1]\}. \quad (14)$$

Here I is the position of the center of the interface and λ_1 is an interface broadening parameter that takes account not only of interfacial diffusion and surface roughness, but also the possible decrease of the Ho moment near the interface. The spacing between successive planes in the model is given by a modification of Eq. (8), which for this choice of origin becomes

$$d_l = \frac{(d_Y + d_{\text{Ho}})}{2} + \frac{(d_Y - d_{\text{Ho}})}{2} \tanh[(l - I)/\lambda_2]. \quad (15)$$

The change in the magnetic turn angle of moments in successive planes is

$$\beta_l = \frac{(\psi_Y + \psi_{\text{Ho}})}{2} + \frac{(\psi_Y - \psi_{\text{Ho}})}{2} \tanh[(l - I)/\lambda_3], \quad (16)$$

where ψ_{Ho} and ψ_Y are the turn angles appropriate to the center of large blocks of Ho and Y, respectively. Thus the total phase of the layer is

$$\phi_l^{\pm} = \sum_{i=1}^l (Qd_i \pm \beta_i). \quad (17)$$

This model assumes that the origin is at the center of a Ho block; equivalent formulas can be derived if it as-

sumed that the block center is midway between two Ho planes. This leads to different intensities for the superlattice Bragg reflections, but for wave-vector transfers that are close to the values at which the maximum intensity occurs, these differences are small. The data to be discussed in Sec. IV span a sufficiently limited range of Q that we are unable to distinguish between the two possibilities. This model has a number of advantages over that used for the x-ray data. For example, if we place no restriction on I being integral, then it is easy to obtain the one-bilayer scattering for noninteger values of $(n_{\text{Ho}} + n_{\text{Y}})$. Even though in this case there is no longer strict periodicity this was found to make a negligible difference to the calculated scattering intensities. The model was used in a two-stage approach to find the unknown parameters. From the terms involving a sum over m in Eq. (12), the magnetic peaks are generated at positions $Q_{\pm} = (2\pi m/L \pm \Phi/L)$. The separation of the magnetic peaks gives L , the bilayer repeat length, while the offset of the magnetic peaks from the position of the nuclear superlattice peaks gives Φ (modulo 2π), because $(Q_N - Q_-) = \Phi/L$. In practice, the peak positions were fitted to a linear form to give both L and Φ . From a fit to the intensity of the peaks of the structure factor values for the turn angles in the two materials ψ_{Ho} and ψ_{Y} and the layer thickness I can be found. Then, as L , d_{Ho} , and d_{Y} are all known, the number of Y atoms can be calculated.

III. SAMPLE GROWTH AND CHARACTERIZATION

The series of Ho/Y superlattice samples was grown by MBE using a Balzers UMS 630 facility. The growth techniques used follow the procedures developed by Kwo *et al.*¹³ The rare-earth metals grow epitaxially onto a Nb metal layer deposited on a sapphire substrate; the Nb acts as a chemical buffer to prevent reaction between the rare earths and sapphire. The body-centered-cubic Nb and the hexagonal-close-packed rare-earth metals grow with their respective close-packed atomic planes parallel to the substrate plane. The epitaxial relationships are $\{110\} \text{Al}_2\text{O}_3 \parallel \{110\} \text{Nb} \parallel \{001\} \text{Y, Ho}$. A Y seed layer is then grown on the Nb buffer of $\approx 1000 \text{ \AA}$. This is above the critical thickness at which the Y lattice relaxes back to its bulk value. The Ho/Y superlattice is then grown on this seed layer. A growth temperature of 300°C is used for the superlattice, a temperature chosen to be low enough to minimize bulk interdiffusion at the Ho/Y interfaces while allowing sufficient surface diffusion to promote a layer-by-layer growth mode (at a growth rate of $\approx 0.5 \text{ \AA/s}$) and hence well-defined interfaces. Finally, a capping layer of Y of thickness $\approx 300 \text{ \AA}$ is grown to inhibit oxidation of the superlattice when exposed to air. Figure 1 is a schematic diagram of a superlattice sample.

The crystalline structure of the superlattice films was investigated using a triple-crystal x-ray diffractometer mounted on a Stoe rotating anode generator operating at 6 KW. By using a channel-cut Ge (111) monochro-

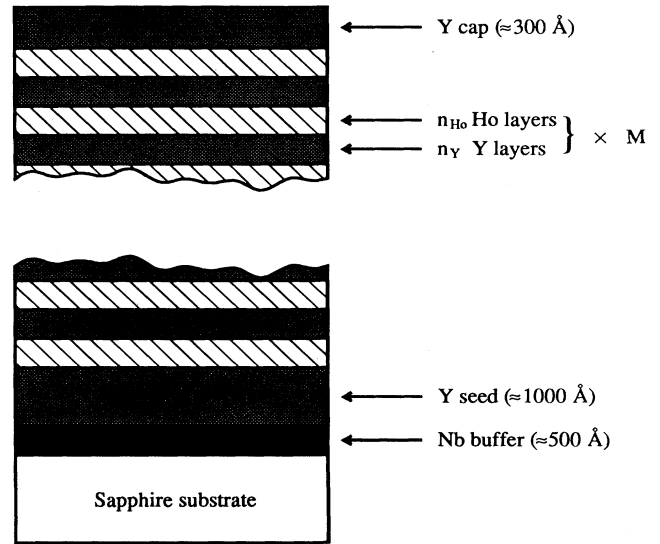


FIG. 1. A schematic diagram of a superlattice sample. The sapphire substrate has a surface area of 1 cm^2 and is 0.5 mm thick.

mator followed by an accurately positioned knife edge, a well-defined incident beam of $\text{Cu } K\alpha_1$ radiation was obtained. After diffracting from the sample, this radiation was collected by a Ge (111) analyzer crystal, before being detected by a gas-proportional counter. With this configuration the wave-vector resolution in the scattering plane, as determined from measurements on a Si (001) crystal, was typically $8 \times 10^{-4} \text{ \AA}^{-1}$ parallel to the x-ray wave-vector transfer and $5 \times 10^{-4} \text{ \AA}^{-1}$ in the transverse direction. In order to characterize the superlattices two different types of measurements were performed.

First, a two-dimensional scan of \mathbf{Q} around a principal Bragg peak was made. From this we can ascertain the degree of crystalline order in the sample. Figure 2 shows the scattering around the (002) Bragg peak for the sample of nominal composition $(\text{Ho}_{40}/\text{Y}_{15})_{50}$. In the transverse direction all the peaks are well defined, corresponding to a high degree of order within the plane. A convenient figure of merit for this is the width of the principal Bragg peak observed in a rocking curve. This particular sample has a rocking-curve width of 0.19° . For \mathbf{Q} parallel to the superlattice modulation direction a series of satellites are observed. These are the superlattice peaks. Satellites up to fourth order are visible, indicating that there is a good superlattice structure in the growth direction. From the width of the central peak in this direction we can obtain an estimate for the structural coherence length. For this sample it is measured to be 1800 \AA .

Second, we accurately scanned the wave-vector transfer \mathbf{Q} parallel to the superlattice modulation direction, for the range of \mathbf{Q} required to include all the superlattice peaks on either side of the (002) Bragg peak visible in Fig. 2. From this the positions and intensities of the superlattice satellites were determined. This information enables the average bilayer length and the average

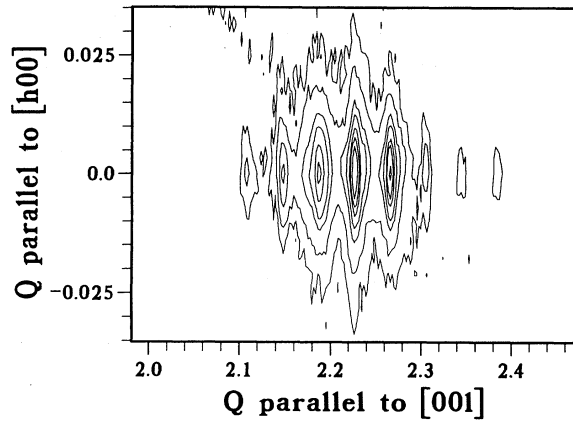


FIG. 2. Intensity contour plot of the x-ray scattering measured in a grid scan of the wave-vector transfer around the (002) Bragg peak. The contours are on a logarithmic scale and the units of Q are \AA^{-1} .

interface width to be determined by using the model developed in Sec. II A. An example of this process, again for the sample with nominal composition $(\text{Ho}_{40}/\text{Y}_{15})_{50}$, is illustrated in Fig. 3, which shows both the measured scattering and the calculated scattering intensity profile obtained by a least-squares fit to these data using the model.

Despite the simplicity of the model, the qualitative agreement with the experimental data is very good. Where the two profiles do differ, however, is that the observed high-order satellites broaden with increasing order. This is a consequence of random fluctuations about the mean bilayer repeat length.¹⁴ Because the random fluctuations also cause a reduction in intensity of the high-order satellites, the interface parameter derived from our model is somewhat large and so may be thought of as an upper bound for the width of the interface region.

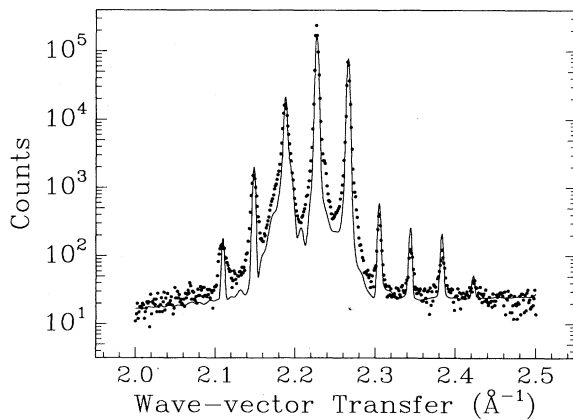


FIG. 3. X-ray scattering from the $(\text{Ho}_{40}/\text{Y}_{15})_{50}$ superlattice in a scan of wave-vector transfer along $[00\ell]$ at room temperature. The points are experimental data and the solid line is a simulation using the model described in Sec. II A, with the parameters given in Table I.

We discuss this at more length in a separate paper,¹⁵ which deals in detail with aspects of the crystalline structure of the superlattices.

In Figs. 4(a) and 4(b), we plot the way the concentration and d spacing change through a bilayer for the $(\text{Ho}_{40}/\text{Y}_{15})_{50}$ sample. The interface extends over some four lattice planes. The c -axis lattice parameter of the Y atomic planes is strained to be greater than the bulk value of 2.865 \AA , while in the Ho blocks the c -axis lattice parameter is smaller than the bulk value of 2.808 \AA . A similar analysis was made on the other samples and the results are summarized in Table I. The interface parameter in the table is the average of the parameters λ_1 and λ_2 defined in Sec. II A. In practice, it is usually sufficient to take the two to be the same. Note that in general there is more strain away from the bulk lattice parameters in the superlattices with thinner blocks of either material. In all the samples the structural coherence length extends across many bilayers and there is only a small mosaic spread in the basal plane. The average coherence length is about 2200 \AA and the average mosaic is about 0.165° . These compare favorably with values reported for other MBE rare-earth superlattices: typical values for the coherence length and mosaic spread of Er/Y superlattices,⁴ for example, were 800 \AA and 0.34° , respectively.

IV. MAGNETIC STRUCTURE

This section contains the results of the neutron-scattering experiments. We begin by discussing briefly the experimental setup. Then, before presenting the results of the study of the superlattice samples, we first consider the results obtained for a 5000 \AA film of Ho. These show how the magnetic properties of strained,

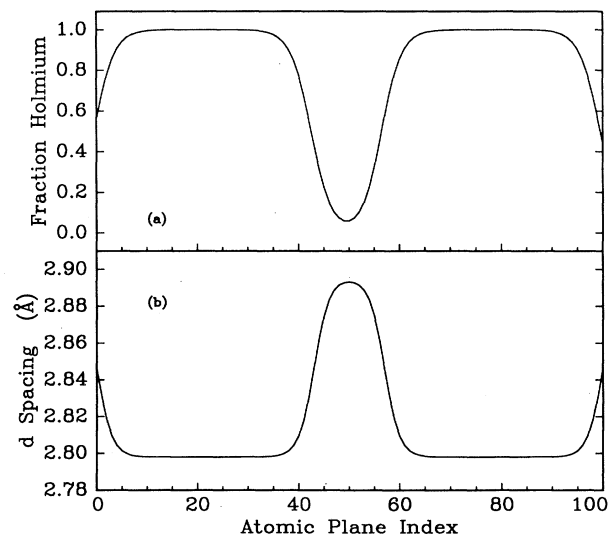


FIG. 4. (a) Concentration profile of holmium for the $(\text{Ho}_{40}/\text{Y}_{15})_{50}$ superlattice used in the simulation of the x-ray scattering shown in Fig. 3. (b) The variation of the d spacing along the c axis in the same superlattice.

TABLE I. The structural parameters of the Ho/Y superlattices as determined by x-ray diffraction at room temperature. The parameters given in the table were obtained from fits to the diffraction profiles by the scattering model described in Sec. II A. The estimated error on the distance between planes along the growth direction is ± 0.005 Å and the error on the interface parameters is ± 0.5 . The superlattice structure is given in the form $(n_{\text{Ho}}/n_{\text{Y}})_M$, where there are M bilayer repeats each with, on average, n_{Ho} atomic planes of Ho and n_{Y} atomic planes of Y.

Nominal structure (Atomic planes)	Measured structure (Atomic planes)	Rocking curve FWHM (Degrees)	Coherence length (Å)	Interplane spacing (Å)	Interface parameter
5000 Å	Ho film	0.20	2560	2.806	–
(6/6) ₁₀₀	6.2/6	0.22	1700	2.785/2.885	5.0
(9/6) ₁₀₀	9.5/5	0.20	1900	2.785/2.885	5.5
(6/15) ₈₀	6.5/14.5	0.15	2500	2.800/2.870	4.5
(6/30) ₆₀	7/31	0.12	2600	2.750/2.880	4.0
(20/15) ₇₀	22/14.5	0.17	2700	2.790/2.890	4.0
(40/15) ₅₀	41/16	0.19	1800	2.800/2.885	3.5
(20/30) ₆₀	20/30	0.11	2300	2.790/2.880	4.5

MBE-grown Ho may be different from the bulk material, even before any superlattice effects are introduced.

A. Experimental details

The neutron-scattering experiments were performed at the DR3 reactor at the Risø National Laboratory, Denmark, using the triple-axis spectrometer TAS1. The collimation from reactor to detector was $60'-30'-30'-120'$ and neutrons with an energy of 5 meV were selected by the (002) reflection of a pyrolytic-graphite monochromator. Second-order contamination was eliminated by use of a cooled beryllium-powder filter. A pyrolytic-graphite analyzer was used to ensure that only elastically scattered neutrons entered the detector. The samples were mounted in a closed-cycle cryostat, with the $(h0\ell)$ plane in the scattering plane. Temperatures in the range 10–300 K could be reached with an accuracy of ± 0.1 K. The wave-vector resolution was measured to be approximately 0.01 \AA^{-1} in the scattering plane. The construction of the spectrometer meant that the maximum wave-vector transfer Q that could be reached along $[00\ell]$ with 5-meV neutrons was 2.35 \AA^{-1} . Thus only the magnetic peaks on the low- Q side of the (002) nuclear Bragg reflection could be observed.

B. Holmium film

Bulk Ho has two distinct ordered phases.¹⁶ Between 132.2 K and about 18 K the moments form a basal-plane spiral. Below 18 K the moments are aligned in a commensurate cone structure, with a helical ordering of wave vector $(1/6) \mathbf{c}^*$ in the basal plane and a small constant ferromagnetic component along the c axis. At high temperatures the helical arrangement of the moments is regular and there is a constant angle between successive moments. At low temperatures the hexagonal basal-plane anisotropy increases rapidly and the moments tend to be pulled towards the nearest b axis and in the cone phase the basal-plane components of the mo-

ments are all bunched in pairs about the easy directions. For temperatures between 18 K and about 30 K the moments are still, in general, paired about an easy direction, but at regular intervals there are single moments along an easy axis. The spacing between these singlets decreases with increasing temperature. The resulting long-period commensurate structures represent a compromise arrangement that attempts to minimize the anisotropy energy while still having an overall wave vector that is close to the position of the peak in the exchange function $\mathcal{J}(\mathbf{q})$. This spin-slip model of Ho, which was proposed by Gibbs *et al.*,¹⁰ is explained in more detail by Cowley and Bates.¹¹ Bunching of the moments about the easy axes and the formation of commensurate structures are readily detected in a neutron-scattering experiment: bunching gives rise to satellites at positions corresponding to five and seven times the underlying wave vector of the modulation, while the commensurate structures may introduce additional higher-order harmonics to the scattering.

By measuring the temperature dependence of the intensity of the principal magnetic satellite of the (002) Bragg peak, the moments in the Ho film were found to order at $T_N = 131.3(0.2)$ K, which is 0.9 K lower than the bulk. A series of scans of the wave-vector transfer along $[00\ell]$ for ℓ between 0.9 and $2.05 \mathbf{c}^*$ were taken at temperatures between 10 K and 50 K. Figure 5 shows the scattering measured at 10 K. The primary magnetic satellite is positioned at $\mathbf{Q} = 1.805(0.003) \mathbf{c}^*$, corresponding to a helical wave vector of $\mathbf{q} = 0.195 \mathbf{c}^*$. This is larger than the value of $(1/6) \mathbf{c}^*$ which occurs at this temperature in the bulk material.¹⁷ Also evident in Fig. 5 is that there are weak peaks at positions given approximately as $\mathbf{Q} = 0.95, 1.00, 1.05, 1.33,$ and 1.4 , all in units of \mathbf{c}^* . These may be indexed as the fifth and seventh harmonics of phases with underlying wave vectors 0.19 and $0.20 \mathbf{c}^*$. The labels on Fig. 5 identify each peak with the appropriate phase. Thus the magnetic structure at low temperatures consists of two distinct phases and although at the position of the primary magnetic satellites there is insufficient resolution to separate these peaks, at the fifth and seventh harmonics they are readily resolved. The data in Fig. 5 suggest that there is about twice as much of the $\mathbf{q} = 0.19 \mathbf{c}^*$ phase

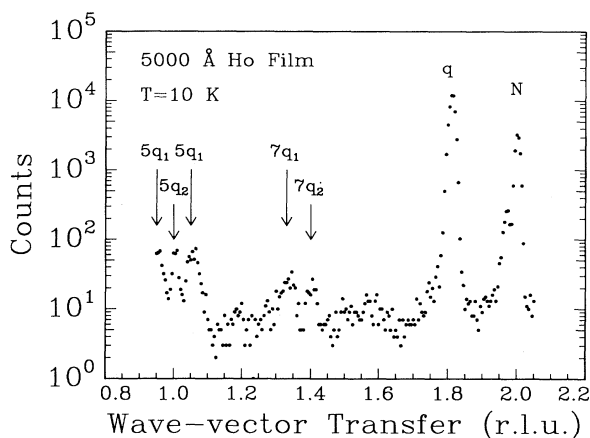


FIG. 5. The neutron scattering observed from the 5000 Å of Ho film in a scan of wave-vector transfer along the $[00\ell]$ direction at a temperature of 10 K. The peak at (002) is nuclear scattering, whereas the other peaks are magnetic in origin. Peaks labeled q_1 are harmonics of the phase with $\mathbf{q}=(4/21)\mathbf{c}^*$ and those labeled q_2 are harmonics of the phase with $\mathbf{q}=(1/5)\mathbf{c}^*$.

as the $0.20\mathbf{c}^*$ phase. These extra satellites show that the magnetic structure is not a simple helix at low temperatures, and instead the hexagonal anisotropy produces bunching near the easy axes. The wave vectors of the helices may be explained if at low temperatures the moments form spin-slip structures similar to those found in bulk Ho at higher temperatures. One of these spin-slip structures has the moments arranged with the singlet moments separated by three pairs of moments, $(2,2,2,1\dots)$, which has a wave vector of $\mathbf{q}=0.1905$ or $(4/21)\mathbf{c}^*$, while the other spin-slip structure has the singlet moments separated by two pairs of moments, $(2,2,1\dots)$, which has a wave vector of $\mathbf{q}=(1/5)\mathbf{c}^*$.

These results show that the MBE-grown Ho film has a magnetic structure which is very different from the bulk. Not only is the the low-temperature $(1/6)\mathbf{c}^*$ phase suppressed and spin-slip structures are instead formed, but also there is a coexistence of the spin-slip phases on a scale not observed under ambient conditions in conventionally grown crystals. In Sec. V we discuss the possibility that these differences are a result of the strain induced by the lattice mismatch between Ho and Y.

C. Superlattices

We now turn our attention to the superlattice samples. We begin by discussing in detail the results for the sample with nominal composition $(\text{Ho}_{40}/\text{Y}_{15})_{50}$. These illustrate the general nature of the magnetic ordering and how it changes with temperature. We then present the results for all the other samples, to show how the magnetic structures depend on different Ho and Y block lengths. Finally, from a study of the high harmonics, we demonstrate that at low temperature the moments form spin-slip structures.

1. The $(\text{Ho}_{40}/\text{Y}_{15})_{50}$ superlattice

Figure 6 shows a series of scans of the wave-vector transfer \mathbf{Q} taken along $[00\ell]$ between 10 K and 130 K at 10 K intervals. At 130 K only the nuclear scattering is observed, with the primary chemical satellites clearly visible. By 120 K the sample is ordered and there is a magnetic side band. There are three features to note in the temperature dependence of the magnetic scattering. (i) The intensity of the magnetic scattering increases strongly with decreasing temperature. This increase shows that the magnetic moments are steadily becoming more ordered as the temperature decreases. (ii) The magnetic side band move towards the nuclear peak as the temperature decreases. This shows that the average turn angle per atomic plane in the helix decreases with decreasing temperature. (iii) The magnetic side band is not a single broad peak, but instead consists of a series of satellites. The presence of these separate magnetic satellites indicates that the magnetic ordering is coherent across the nonmagnetic Y blocks. The separation between these superlattice peaks is determined by the bilayer repeat length. Moreover, this substructure is present at all temperatures. Thus as soon as the Ho moments in the individual blocks order, then they are simultaneously coupled to successive blocks.

A more detailed description of this structure, in particular a determination of the individual turn angles in the Ho and the Y blocks, may be obtained only by fitting the results to a model, and we now describe the way this was achieved. Initially, the positions and intensities of the magnetic peaks were obtained by fitting a Gaussian to each of the peaks. The positions of the magnetic peaks were then compared with that of the superlattice nuclear peaks to obtain the magnetic turn angle per bilayer, or Φ in the notation introduced in Sec. II B. The results are

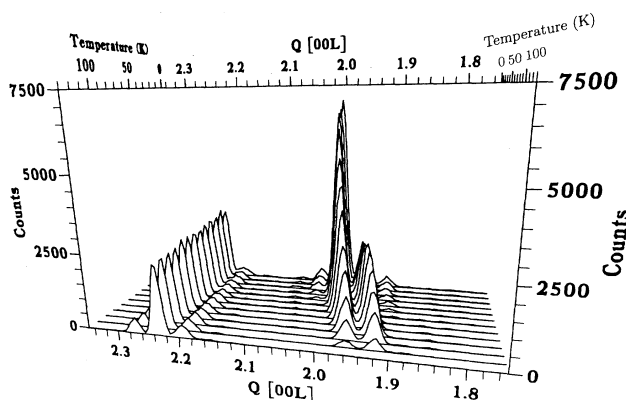


FIG. 6. The temperature dependence of the neutron scattering along $[00\ell]$ observed from the $(\text{Ho}_{40}/\text{Y}_{15})_{50}$ superlattice. The scans were taken successively at temperature intervals of 10 K between 130 K and 10 K. The scan in the foreground picture was taken above the Néel temperature and hence only the nuclear scattering, including the superlattice sidebands, is evident near $Q=2.23\text{ \AA}^{-1}$.

TABLE II. The magnetic properties of the Ho/Y superlattices. The total turn angle per bilayer was measured from the average separation between the magnetic and nuclear peaks. The average turn angle between atomic planes in the holmium and the yttrium, ψ_{Ho} and ψ_{Y} , are determined from a fit of the data to the model described in Sec. II B.

Nominal structure (Ho/Y)	Ordering temperature (K)	Turn angle per bilayer at 10 K (Degrees)	Turn angle at 10 K in Ho (Degrees)	Turn angle at 10 K in Y (Degrees)	Turn angle at ordering in Ho (Degrees)
5000 Å film	131.3(0.3)	—	35.0(0.5)	—	50.0(1.0)
(40/15)	127(1.0)	2408(20)	39.3(0.5)	51.1(1.0)	50.0(2.0)
(20/30)	115(1.0)	2451(30)	41.9(1.0)	49.7(1.0)	49.5(2.0)
(20/15)	117(1.0)	1645(20)	42.8(0.8)	48.6(2.0)	50.5(2.0)
(9/6)	110(1.0)	655(20)	45.5(1.5)	49.7(2.0)	51.0(2.0)
(6/30)	87(2.0)	1029(20)	47.5(2.5)	49.3(1.0)	49.5(3.0)
(6/15)	84(2.0)	605(20)	49.0(1.5)	49.0(3.0)	50.0(3.0)
(6/6)	95(2.0)	1858(20)	45.4(2.0)	53.8(3.0)	50.5(3.0)

listed in Table II. The intensities of the magnetic peaks were then used to obtain the parameters of the model discussed in Sec. II B by fitting A_H , the turn angles ψ_{Ho} , $(\psi_{\text{Y}} - \psi_{\text{Ho}})$, the Ho layer thickness $2I$, and the interface widths. It was found that good fits to the intensities could be obtained, but that the fits were largely insensitive to the difference in the turn angles, $(\psi_{\text{Y}} - \psi_{\text{Ho}})$. This is not surprising: there is no scattering from the Y, so this term contributes in the interface region only. In many of the trial fits, therefore, ψ_{Y} was held to be the same as ψ_{Ho} . The value of ψ_{Ho} obtained in the fit was then used with the measured value of the total bilayer turn angle Φ to determine ψ_{Y} . The block lengths and interface widths were consistent with the values found from the x-ray measurements. For example, for this sample of nominal parameters $(\text{Ho}_{40}/\text{Y}_{15})_{50}$, the number of Y planes was determined to be 16 with x rays and 15.7 with neutrons, while the interface width was 3.5(0.5) with x rays and 4.0(0.5) with neutrons. Furthermore, in the analysis of the magnetic peaks as a function of temperature these parameters did not change with temperature. Thus the Ho block length and interface width were held at the values obtained from our x-ray measurements.

These findings support the model described in Sec. II B as being the correct description of the magnetic structure. If the moments at the edges of a Ho block had a different magnitude to those in the center of the block, or if they were more disordered, then we would expect the magnetic and chemical data to give different values for the Ho block size and interface width. That this did not occur implies all the Ho^{3+} moments are equally developed and ordered, and any edge effects are determined solely by the crystallographic structure. As a check on the procedure described above, the magnetic scattering was also calculated directly, convoluted with the resolution and the parameters obtained from a fit to the whole of the measured spectra. There were no significant differences in the results obtained by the two procedures, but the former was more convenient for computation.

An example of the results obtained from the fitting process is illustrated in Fig. 7, which shows the observed and calculated scattering from the $(\text{Ho}_{40}/\text{Y}_{15})_{50}$ at 10 K. It is clear that the model gives a good account of the

magnetic scattering over many decades of intensity. This procedure was repeated for scans made at a series of temperatures, and the results obtained for the parameters of the model for the $(\text{Ho}_{40}/\text{Y}_{15})_{50}$ sample are summarized in Figs. 8 and 9. In Fig. 8 the turn angle between successive Ho planes is shown as a function of temperature, and is compared with that of the Ho film discussed in Sec. III A and bulk Ho.¹⁰ The turn angle increases with increasing temperature and is always greater in the superlattice than in pure Ho. At temperatures below about 30 K, the turn angle in the Ho becomes almost constant, and has a value of $\approx 40^\circ$. The turn angle between successive Y planes is seen to be independent of temperature. The parameter A_H , the magnetic scattering amplitude, is a measure of the size of the moment on the Ho atoms. Figure 9 shows the temperature dependence of the magnetization of the Ho blocks; it increases steadily with decreasing temperature.

2. General trends

Similar measurements were performed with the other superlattices, although the temperature dependence was

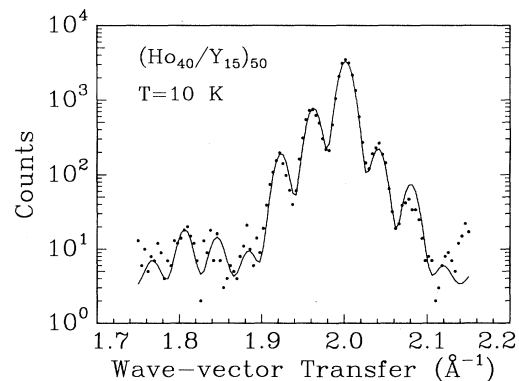


FIG. 7. The neutron scattering for the $(\text{Ho}_{40}/\text{Y}_{15})_{50}$ superlattice measured in a scan of the wave-vector transfer along $[00\ell]$ at 10 K. The points are the experimental data and the solid line is a fit using the model described in Sec. II B.

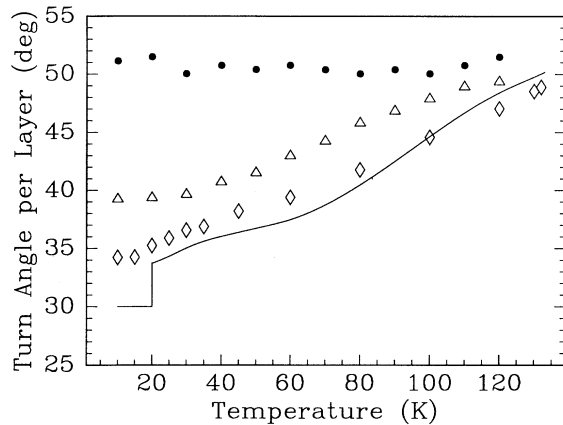


FIG. 8. The temperature dependence of the turn angle in the Ho (Δ) and Y (\circ) for the $(\text{H}_{40}/\text{Y}_{15})_{50}$ superlattice. Also shown is the measured turn angle in the 5000- \AA holmium film (\diamond). The solid line is the turn angle measured in bulk Ho (Ref. 10).

studied in less detail. In every case the model detailed in Sec. III B gives a good account of the results, including samples with thin blocks of Ho, as is shown in Fig. 10. The results for the magnetic structures of all the samples are summarized in Table II. A number of trends are evident. The average turn angle between the Y planes at 10 K for all the superlattices is found to be $50.2(1.5)^\circ$ and is in every case independent of temperature. The average turn angle between the Ho planes upon ordering, $50.0(2.5)^\circ$, is essentially the same for all the samples. It then decreases as the temperature decreases and the ordered moment increases. The turn angle in the Ho blocks at 10 K decreases as the Ho thickness increases, and is largely independent of the length of Y blocks, as is shown in Fig. 11. The ordering temperature T_N decreases with decreasing Ho layer thickness, and is not sensitive to

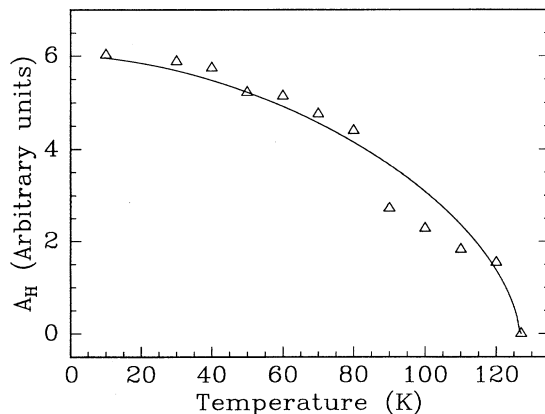


FIG. 9. The temperature dependence of the magnetic scattering amplitude A_H for the $(\text{H}_{40}/\text{Y}_{15})_{50}$ superlattice. The solid line is a guide to the eye.

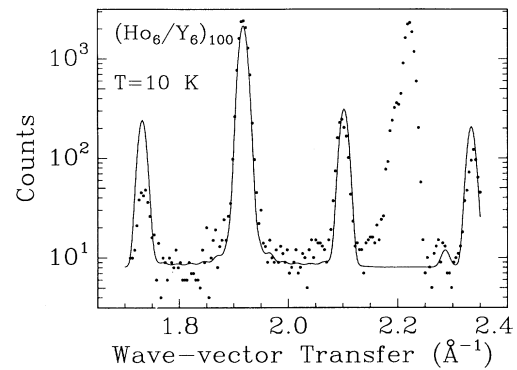


FIG. 10. The neutron scattering from the $(\text{Ho}_6/\text{Y}_6)_{100}$ superlattice measured in a scan of the wave-vector transfer along $[00\ell]$ at 10 K. The points are experimental data and the solid lines are a fit using the model of Sec. II B. The peaks near $Q=2.2 \text{ \AA}^{-1}$ are due to nuclear-scattering processes.

the thickness of the Y blocks, as is illustrated in Fig. 12. The decrease with decreasing Ho block length is initially fairly smooth, but then it begins to decrease fairly rapidly for block lengths of nine or fewer Ho atoms.

In addition to a study of the basal plane ordering, for many of the samples a search was made for a c -axis moment, but no net c -axis moment was observed in any of the samples studied. To determine whether the low-temperature helix is confined to the basal plane or whether it is tilted out of the basal plane, scans along $[10\ell]$ were made for the $(\text{Ho}_{40}/\text{Y}_{15})_{50}$ superlattice, but there was no evidence for an oscillating c -axis moment. Therefore, our results suggest that the helix is confined mainly to the basal plane at all temperatures. It is possible that if the opening angle of the cone or the tilted helix is small, then the resulting c -axis moment might be too small to have been detected in this experiment. Further work is in progress to investigate the presence of any c -axis moment.

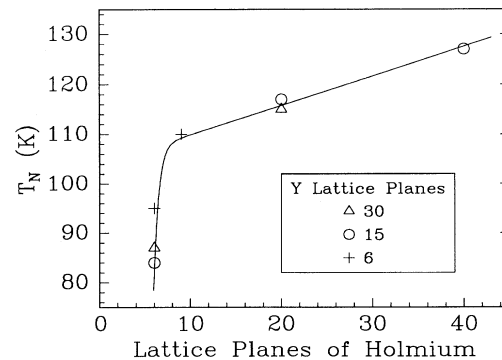


FIG. 11. The turn angle between successive moments in the holmium blocks in the superlattices at 10 K, as a function of the length of the holmium block. The solid line is a guide to the eye.

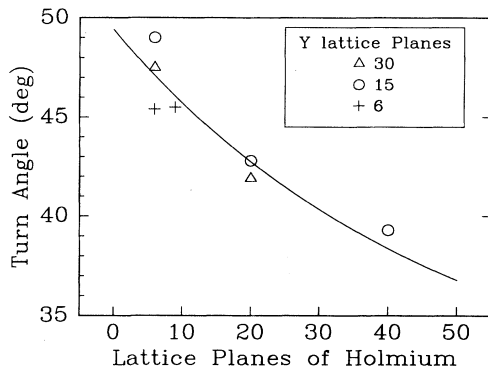


FIG. 12. The temperature at which the holmium moments in the superlattices order as a function of the length of the holmium block. The solid line is a guide to the eye.

3. Spin-slip structures

In addition to the primary satellites, higher-order harmonics were observed from some of the superlattices. Figure 13 shows some higher-order harmonics from the $(\text{Ho}_{40}/\text{Y}_{15})_{50}$ superlattice. These are identified as the fifth harmonics of (000) and (002) . There are three important features about these peaks: (i) the scattering is a broad peak that has none of the fine structure evident in the primary peak, (ii) they are at positions corresponding to an average turn angle of $39.8(1.0)^\circ$, and (iii) the average ratio of the integrated intensities of the fifth and first harmonics is $0.0030(5)$, compared to $0.0065(5)$ in the bulk.¹⁷ The presence of these peaks indicates that the helix is not smooth; there is bunching about the six easy directions in the basal plane. For there to be bunching and have an average turn angle of $\approx 40^\circ$, then the moments cannot be arranged either in the manner found in bulk Ho at low temperatures or in the way predicted for thick free-standing Ho block.⁹ Both

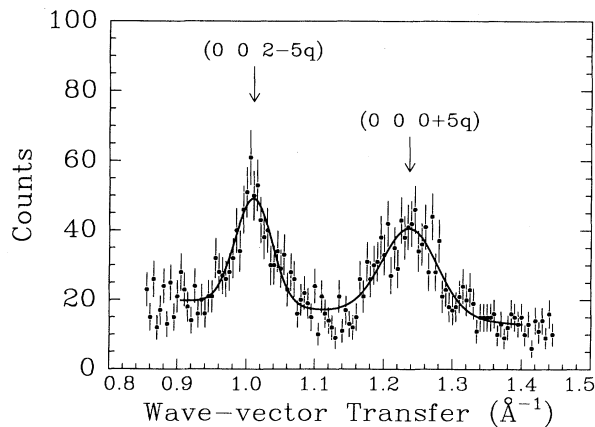


FIG. 13. The fifth harmonics of the $(\text{Ho}_{40}/\text{Y}_{15})_{50}$ superlattice. The points are experimental data and the solid line is a fit to two Gaussians and a sloping background.

of these arrangements have most of the moments bunched in pairs about the easy axes, and therefore have an average turn angle that is too small. Instead there must be a combination of singlets and doublets and thus at low temperatures the moments in the superlattices form commensurate spin-slip structures. An arrangement that has the correct average turn angle of 40° is the $\mathbf{q}=(2/9)\mathbf{c}^*$ spin-slip structure. This structure, which has alternating singlets and doublets or $(2,1,2,1\dots)$, gives rise to first, fifth, and seventh harmonics only. The seventh harmonics of (002) and (000) occurred at positions that were close to the straight through beam and the tail of the primary magnetic sideband, respectively, so no useful information could be gained from these peaks. However, from the measured ratio of the fifth and first harmonics we have calculated that the bunching angle that the moments make with the nearest easy axis is $15(2)^\circ$, compared to 20° in the undistorted helix with the same average turn angle. The basal-plane arrangements of the moments in this structure and in bulk Ho at the same temperature are shown in Fig. 14.

The average width of the fifth harmonics indicates a correlation length of $80(8)\text{ \AA}$, a value close to the length of one Ho block ($\approx 115\text{ \AA}$). This contrasts to the correlation length of $651(65)\text{ \AA}$ determined from the widths of the primary satellites. The difference between these widths implies that while the chirality and average turn angle in the Ho is preserved across the Y, no information about the position of the singlets and doublets is transmitted. Consequently, the position of the fifth harmonics depends only on the turn angle in the Ho blocks and so this provides an independent check on the value of the Ho average turn angle determined from the fit of the model to the primary satellite. The fact that the two values agree very well means we can be confident that the values for the turn angles found from the model are correct.

Fifth harmonics were also observed for the $(\text{Ho}_{20}/\text{Y}_{15})_{70}$ sample. They were weak, but again consisted of a single, broad peak. Their widths indicate a correlation length of $54(5)\text{ \AA}$, compared to the Ho block length of $\approx 62\text{ \AA}$. A possible spin-slip structure for the

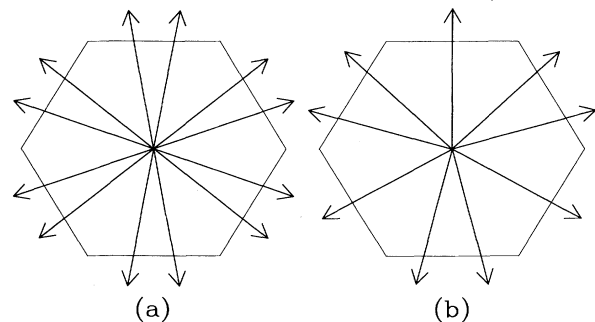


FIG. 14. The arrangements of the basal-plane components of the moments at low temperatures in (a) the $\mathbf{q}=(1/6)\mathbf{c}^*$ structure of bulk Ho and in (b) the $\mathbf{q}=(2/9)\mathbf{c}^*$ spin-slip structure found in the $(\text{Ho}_{40}/\text{Y}_{15})_{50}$ superlattice.

Ho blocks in this sample, which has an average turn angle close to the measured value of $43(0.5)^\circ$, is $(2,1,2,1,1\dots)$. No high harmonics were observed in the samples with Ho blocks of six planes Ho. This is not too surprising: because the width of the high harmonics is inversely proportional to the block length, then they would be too weak to be detected in this experiment. Nevertheless, the large hexagonal basal-plane anisotropy at low temperatures means that the moments must be bunched about the easy axes and so are expected to form commensurate structures. Table III shows the average turn angles for a series of spin-slip structures. Comparison with Table II shows that the average turn angle at low temperatures of all the superlattices may be explained by one of these spin slip-structures. Many of these spin-slip structures with $b \leq 3$ are not seen in bulk Ho, because at the high temperatures where the average turn angles are close to that required by the exchange, then the effect of the hexagonal anisotropy is small and thus spin-slip structures are not formed.

V. DISCUSSION

The previous section presented a detailed account of the magnetic structures that are formed in Ho/Y superlattices. In this section we discuss some of the reasons why the Ho in our MBE samples behaves differently from bulk Ho. The results show that the magnetic structure of the Ho, in both the superlattices and in the 5000 Å film, is different from that of the bulk in two main ways. First, the ordering temperature is reduced and second, the turn angle is always larger than in bulk Ho, particularly at low temperatures. This behavior is qualitatively similar to that observed in bulk Ho under hydrostatic pressure. Umabayashi *et al.*¹⁸ have shown that pressure reduces the ordering temperature by $3.3(0.5)$ K/GPa, while Kawano *et al.*¹⁹ have found that pressure increases the average turn angle at low temperatures. Thus it is plausible that the strain introduced by the lattice mismatch between the Ho and Y is responsible for the changes in the ordering temperature and low-temperature turn angle observed in our samples. The strains introduced by the epitaxial growth of Ho on Y in the MBE samples are highly anisotropic: the Ho is expanded in the basal plane, but the c -axis lattice parameter is contracted. Unfortu-

TABLE III. Average turn angles in selected spin-slip structures.

Spin-slip structure	Average turn angle
2,1,2,1...	40.0
2,1,2,1,1...	42.9
2,1,1,2,1,1...	45.0
2,1,1,2,1,1,1...	46.7
2,1,1,1...	48.0
2,1,1,1,1...	50.0
2,1,1,1,1,1...	51.4

nately, there have been no studies investigating the effect of anisotropic stresses on T_N and the low-temperature turn angle, but by using the elastic constants of Ho determined by Palmer and Lee,²⁰ the strain along the c axis, ϵ_{33} , produced by isotropic pressure may be found, and is calculated to be -0.0086 /GPa. We have then used the value of dT_N/dP measured by Umabayashi *et al.*¹⁸ to calculate the value of ϵ_{33} that would be required to produce the measured shift in T_N in our samples if it were a function of the c -axis strain only. Similarly, we have calculated the strain required to produce the low-temperature turn angles observed by Kawano *et al.*¹⁹ The results of this process for the 5000 Å film and some of the superlattices are shown in Table IV. There are three points to note. (i) The strains predicted by the two sets of measurements on the bulk give similar values for each sample, even though the strains themselves vary over an order of magnitude. (ii) The measured strains are always smaller than the predicted strains. This systematic difference may arise because we are comparing the effect of isotropic pressure with anisotropic stresses and indicates that the change to the basal-plane strain as well as the c -axis strain might be significant in altering the magnetic behavior of the Ho. However, the fact that the measured strains are of the same order of magnitude as the calculated ones for a wide range of stresses suggests that the c -axis strain has an important bearing on the magnetism. (iii) The factors by which the measured strains are different from the average predicted strains are similar. In particular, the factors for the Ho film and the $(\text{Ho}_{40}/\text{Y}_{15})_{50}$ sample, ≈ 3 and 5 , respectively, are close even though they are quite different in nature: one is

TABLE IV. The measured values of the c -axis strain and the values calculated from hydrostatic pressure measurements. The strains in the column headed T_N are calculated from the value of dT_N/dP measured by Umabayashi *et al.* (Ref. 18) and the values in the column headed ψ_{Ho} at 10 K are based on the low-temperature turn angles measured by Kawano *et al.* (Ref. 19).

Sample	Measured	Strain ϵ_{33}	
		Calculated from:	
		T_N	ψ_{Ho} at 10 K
Ho film	-0.0007(2)	-0.0023(5)	-0.0035(5)
$(\text{Ho}_{40}/\text{Y}_{15})_{50}$	-0.0032(10)	-0.014(5)	-0.014(5)
$(\text{Ho}_{20}/\text{Y}_{15})_{70}$	-0.0065(15)	-0.040(10)	-0.030(10)
$(\text{Ho}_{20}/\text{Y}_{30})_{60}$	-0.0065(15)	-0.040(10)	-0.030(10)

pure Ho, the other a superlattice.

These observations lead us to the conclusion that the changes to the magnetism in the $(\text{Ho}_{40}/\text{Y}_{15})_{50}$ sample are determined only by the properties of the Ho blocks, in particular the strain. The Y blocks have a negligible effect on the ordering temperature and the low-temperature turn angle in the $(\text{Ho}_{40}/\text{Y}_{15})_{50}$ superlattice, other than introducing strain. This hypothesis, that the magnetism depends only on the state of the Ho blocks and not on the Y, is further supported by the observation that the $(\text{Ho}_{20}/\text{Y}_{15})_{70}$ and $(\text{Ho}_{20}/\text{Y}_{30})_{60}$ superlattices have similar ordering temperatures, as is illustrated in Fig. 12, even though they have different thicknesses of Y separating neighboring Ho blocks. However, the measured c -axis strain is the same in both these samples. Thus we believe that for superlattices with *thick* Ho blocks, the ordering temperature and low-temperature turn angle are essentially those of a strained, free-standing block of Ho. Although the moments at the ends of successive Ho blocks are coupled by the Y, this coupling does not greatly alter the magnetic behavior of the Ho. The coupling through the Y is long ranged, but weak. For the samples with thin blocks of Ho this simple model breaks down. In our superlattices with a Ho block length of less than nine atomic planes the interface region becomes comparable to the whole Ho block. Thus the Ho block is really a Ho-Y alloy of varying composition, and it is this factor that leads to the sudden decrease in T_N illustrated in Fig. 12. The measured ordering temperatures are nevertheless still considerably higher than if the superlattices with thin Ho blocks were completely random alloys. For example, the $(\text{Ho}_6/\text{Y}_6)_{100}$ superlattice orders at 95 K, well above the value of 80 K found in a $\text{Ho}_{0.5}\text{Y}_{0.5}$ random alloy.²¹

While our results suggest that the magnetic ordering in the Ho/Y superlattices is influenced by the strain, it would clearly be desirable to put these effects on a more quantitative footing. The reduction in the ordering temperature of Ho in the superlattices indicates that the height of the peak in $\mathcal{J}(\mathbf{q})$ is reduced by the strain, an effect found in calculations on the effect of hydrostatic pressure on Tb, Dy, and Gd.²² However, the position of the peak in $\mathcal{J}(\mathbf{q})$ appears to be little affected by the strain, because the values of the turn angle in the Ho upon order, shown in Table II, are essentially the same for all the samples. The subsequent change in the turn angle as the temperature is reduced is the result of two factors: the opening of new super-zone gaps created by the periodic potential of the increasing ordered moment²³ and spin-disorder scattering.²⁴ Both of these factors have been incorporated in a free-electron model by Miwa,²⁵ and the theory predicts that the observed change in the low-temperature turn angle results from a reduction in the matrix element of the coupling between the conduction electrons and the localized $4f$ electrons. While this is qualitatively consistent with the observed reduction in $\mathcal{J}(\mathbf{q})$ from the reduction in T_N , a more detailed theory is required to explain simultaneously the observed changes in the ordering temperature and the low-temperature turn angle.

VI. SUMMARY

We have grown a series of Ho/Y superlattices by MBE with a range of Ho and Y block lengths. The x-ray results show that the superlattices are of a high crystallographic quality when compared to other rare-earth superlattices. The mosaic width is typically 0.2° and the spatial coherence length is $\approx 2000 \text{ \AA}$, or about one-half of the superlattice thickness. The interfaces between the Ho and Y blocks are sharp and have a width of about four atomic planes. The neutron-scattering results have been analyzed using a model that assumes there is a helical ordering through both the Ho and Y blocks, with different turn angles in the Ho and the Y. The scattering amplitude and the turn angle in any atomic plane are determined simply by the concentration of the Ho and Y ions in that plane. Fits to the neutron data with this model give the same Ho block length and interface width as found from the x-ray results, showing that the magnetic structure follows closely the crystallographic structure. It is found that the effective turn angle per layer in the Y is the same for all samples, and independent of temperature. The value of the Y turn angle of about 50° is close to that observed in the Y blocks in other superlattice systems^{3,8} and in dilute Y alloys,^{21,26} and is consistent with the calculated peak in the susceptibility of the conduction electrons.²⁷ The temperature at which the Ho moments order and the low-temperature turn angle is reduced in all the samples. These effects are due largely to the strain imposed by the epitaxial growth process, which reduces the height of the peak in $\mathcal{J}(\mathbf{q})$. This model of a simple helical ordering in the Ho, which is equivalent to the one that has been successfully used to describe the magnetic properties of Dy/Y superlattices,³ is sufficient to account for most of the measured scattering. However, in order to explain the presence of higher-order peaks, a more detailed description of the arrangement of the moments is required: at low temperatures there is bunching of the moments about the six easy axes in the basal plane, and the moments form spin-slip structures. The positions of the higher harmonics allow the average turn angle in the Ho blocks to be calculated with no assumptions about the coupling in the Y. A comparison of the widths of the first and fifth harmonics indicates that while the phase and coherence of the helix is preserved across the Y blocks, there is no correlation in the positions of spin-slips in successive Ho blocks.

ACKNOWLEDGMENTS

We have benefited from many useful discussions with A. R. Mackintosh and J. Jensen. We would like to thank the technical staff at Risø for their help in performing these experiments. We are grateful to D. Keen and C. C. Wilson for help with preliminary experiments at ISIS. Financial support for the work at Risø was provided by the E.C. under the Large Scale Facility Program. The work in Oxford was funded by the Science and Engineering Research Council. D.A.J. would like to thank the States of Guernsey Education Council for a grant.

- ¹ C. F. Majkrzak, J. Kwo, M. Hong, Y. Yafet, Doon Gibbs, C. L. Chien and J. Bohr, *Adv. Phys.* **40**, 99 (1991).
- ² R. E. Camley, J. Kwo, M. Hong, and C. L. Chien, *Phys. Rev. Lett.* **64**, 2703 (1990).
- ³ R. W. Erwin, J. J. Rhyne, M. B. Salamon, J. Borchers, Shantanu Sinha, R. Du, J. E. Cunningham, and C. P. Flynn, *Phys. Rev. B* **35**, 6808 (1987).
- ⁴ J. A. Borchers, M. B. Salamon, R. W. Erwin, J. J. Rhyne, R. R. Du, and C. P. Flynn, *Phys. Rev. B* **43**, 3123 (1991).
- ⁵ Y. Yafet, *J. Appl. Phys.* **61**, 4058 (1987).
- ⁶ M. K. Wilkinson, W. C. Koehler, E. O. Wollan, and J. W. Cable, *J. Appl. Phys.* **32**, 48S (1961).
- ⁷ M. Hong, R. M. Fleming, J. Kwo, L. F. Schneemeyer, J. V. Waszczak, J. P. Mannaerts, C. F. Majkrzak, Doon Gibbs, and J. Bohr, *J. Appl. Phys.* **61**, 4052 (1987).
- ⁸ J. A. Borchers, M. B. Salamon, R. W. Erwin, J. J. Rhyne, G. J. Nieuwenhuys, R. R. Du, C. P. Flynn, and R. S. Beach, *Phys. Rev. B* **44**, 11 814 (1991).
- ⁹ J. Bohr, Doon Gibbs, J. D. Axe, D. E. Moncton, K. L. D'Amico, C. F. Majkrzak, J. Kwo, M. Hong, C. L. Chien, and J. Jensen, *Physica B* **159**, 93 (1989).
- ¹⁰ Doon Gibbs, D. E. Moncton, K. L. D'Amico, J. Bohr, and B. H. Grier, *Phys. Rev. Lett.* **55**, 234 (1985).
- ¹¹ R. A. Cowley and S. Bates, *J. Phys. C* **21**, 4113 (1988).
- ¹² *The International Tables for X-ray Crystallography, Volume IV*, edited by James A. Ibers and Walter C. Hamilton (Kynoch, Birmingham, 1974), p. 101.
- ¹³ J. Kwo, E. M. Gyorgy, D. B. McWhan, F. J. DiSalvo, C. Vettier, and J. E. Bower, *Phys. Rev. Lett.* **55**, 1402 (1985).
- ¹⁴ Eric E. Fullerton, Ivan K. Schuller, H. Vanderstraeten, and Y. Bruynseraede, *Phys. Rev. B* **45**, 9292 (1992), and references therein.
- ¹⁵ P. Swaddling and D. F. McMorrow (unpublished).
- ¹⁶ W. C. Koehler, J. W. Cable, M. K. Wilkinson, and F. O. Wollan, *Phys. Rev.* **151**, 414 (1966).
- ¹⁷ G. P. Felcher, G. H. Lander, T. Arai, S. K. Sinha, and F. H. Spedding, *Phys. Rev. B* **13**, 3034 (1976).
- ¹⁸ H. Umebayashi, G. Shirane, B. C. Frazer, and W. B. Daniels, *Phys. Rev.* **165**, 688 (1963).
- ¹⁹ S. Kawano, N. Achiwa, A. Onodera, Y. Nachai, and B. Lebeck (unpublished).
- ²⁰ S. J. Palmer and E. Lee, *Proc. R. Soc. (London) Ser. A* **327**, 519 (1972).
- ²¹ H. R. Child, W. C. Koehler, E. O. Wollan, and J. W. Cable, *Phys. Rev.* **138**, 1655 (1965).
- ²² G. S. Fleming and S.H. Liu, *Phys. Rev. B* **2**, 164 (1970).
- ²³ R. J. Elliott and F.A. Wedgwood, *Proc. Phys. Soc.* **81**, 846 (1963).
- ²⁴ P. G. de Gennes and D. Saint James, *Solid State Commun.* **1**, 62 (1963).
- ²⁵ H. Miwa, *Proc. Phys. Soc. London* **85**, 1197 (1965).
- ²⁶ B. L. Reid, P. W. Mitchell, R. Caudron, B. D. Rainford, M. A. H. McCausland, and A. T. Boothroyd, *Physica B* **174**, 39 (1991).
- ²⁷ S. H. Liu, R. P. Gupta, and S. K. Sinha, *Phys. Rev. B* **4**, 1100 (1971).